Journal of Inflammation Research

Dovepress
Taylor & Francis Group

Open Access Full Text Article

ORIGINAL RESEARCH

Catalpol Alleviates HFpEF via Inhibition of the S100A8-RAGE-NOX4 Inflammatory Axis in Murine Hearts

Yu Cao[1,*], Sudan Li[2,*], Yi Zhang[2], Menghua He[3], Yan Shen[2]

[1]Department of Geriatrics, Yueyang Hospital of Integrated Traditional Chinese and Western Medicine, Shanghai University of Traditional Chinese Medicine, Shanghai, People's Republic of China; [2]Department of Cardiology, Yueyang Hospital of Integrated Traditional Chinese and Western Medicine, Shanghai University of Traditional Chinese Medicine, Shanghai, People's Republic of China; [3]Department of Teaching Affairs, Yueyang Hospital of Integrated Traditional Chinese and Western Medicine, Shanghai University of Traditional Chinese Medicine, Shanghai, People's Republic of China

*These authors contributed equally to this work

Correspondence: Yan Shen, Department of Cardiology, Yueyang Hospital of Integrated Traditional Chinese and Western Medicine, Shanghai University of Traditional Chinese Medicine, Shanghai, People's Republic of China, Email sheny26@126.com

Purpose: This study aimed to elucidate the therapeutic effects of catalpol (CAT) on heart failure with preserved ejection fraction (HFpEF) and explore its underlying mechanisms.

Methods: An HFpEF mouse model was established by combining a high-fat diet with N^ω^-nitro-L-arginine methyl ester administration, followed by CAT treatment for four weeks. Cardiac function was assessed by echocardiography, while histopathological changes were evaluated using hematoxylin–eosin and Masson's trichrome staining. Network pharmacology and transcriptomic analyses were integrated to identify the core targets and signaling pathways of CAT in HFpEF. In vitro, H9C2 were stimulated with angiotensin II (Ang II), followed by CAT treatment, with recombinant rat S100A8 used to specifically activate the TLR4/RAGE pathway. Western blotting (WB) and quantitative real-time PCR were performed to validate the predicted signaling mechanisms both in vivo and in vitro.

Results: In vivo, CAT markedly improved multiple pathological and functional abnormalities in HFpEF mice, including obesity, glucose intolerance, hypertension, diastolic dysfunction, myocardial inflammation, and fibrosis. Integrated network pharmacology and transcriptomic analyses consistently identified the RAGE signaling pathway as the key pathway of CAT. Molecular docking revealed strong binding affinities between CAT and S100A8, RAGE, NOX4, ERK1, and MMP2. WB results further demonstrated that CAT significantly downregulated the S100A8/RAGE/NOX4 axis and its downstream effector MMP2 in cardiac tissue. In vitro, CAT alleviated Ang II–induced cardiomyocyte hypertrophy, reduced the expression of inflammatory cytokines (TNF-α, IL-1β, IL-6) and the heart failure marker ANP, and inhibited S100A8, RAGE, and NOX4 protein levels. Notably, recombinant S100A8 activation weakened the protective effects of CAT.

Conclusion: CAT exerts cardioprotective effects against HFpEF by suppressing myocardial inflammation and fibrosis through modulation of the S100A8/RAGE/NOX4 signaling axis and its downstream effectors.

Keywords: catalpol, heart failure with preserved ejection fraction, network pharmacology, S100A8-RAGE-NOX4 axis, transcriptomics

Introduction

Heart failure with preserved ejection fraction (HFpEF) is a clinical syndrome characterized by impaired diastolic function despite a preserved left ventricular ejection fraction (LVEF ≥ 50%).[1] Currently, approximately 32 million individuals worldwide are affected by HFpEF,[2] and its prevalence continues to rise due to population aging and the increasing burden of cardiovascular and metabolic comorbidities.[3,4] Recent studies have identified inflammation as a key driver in the pathogenesis of HFpEF,[5] promoting pathological cardiomyocyte hypertrophy, myofibroblast proliferation, and

Received: 10 July 2025
Accepted: 28 November 2025
Published: 8 December 2025

Graphical Abstract

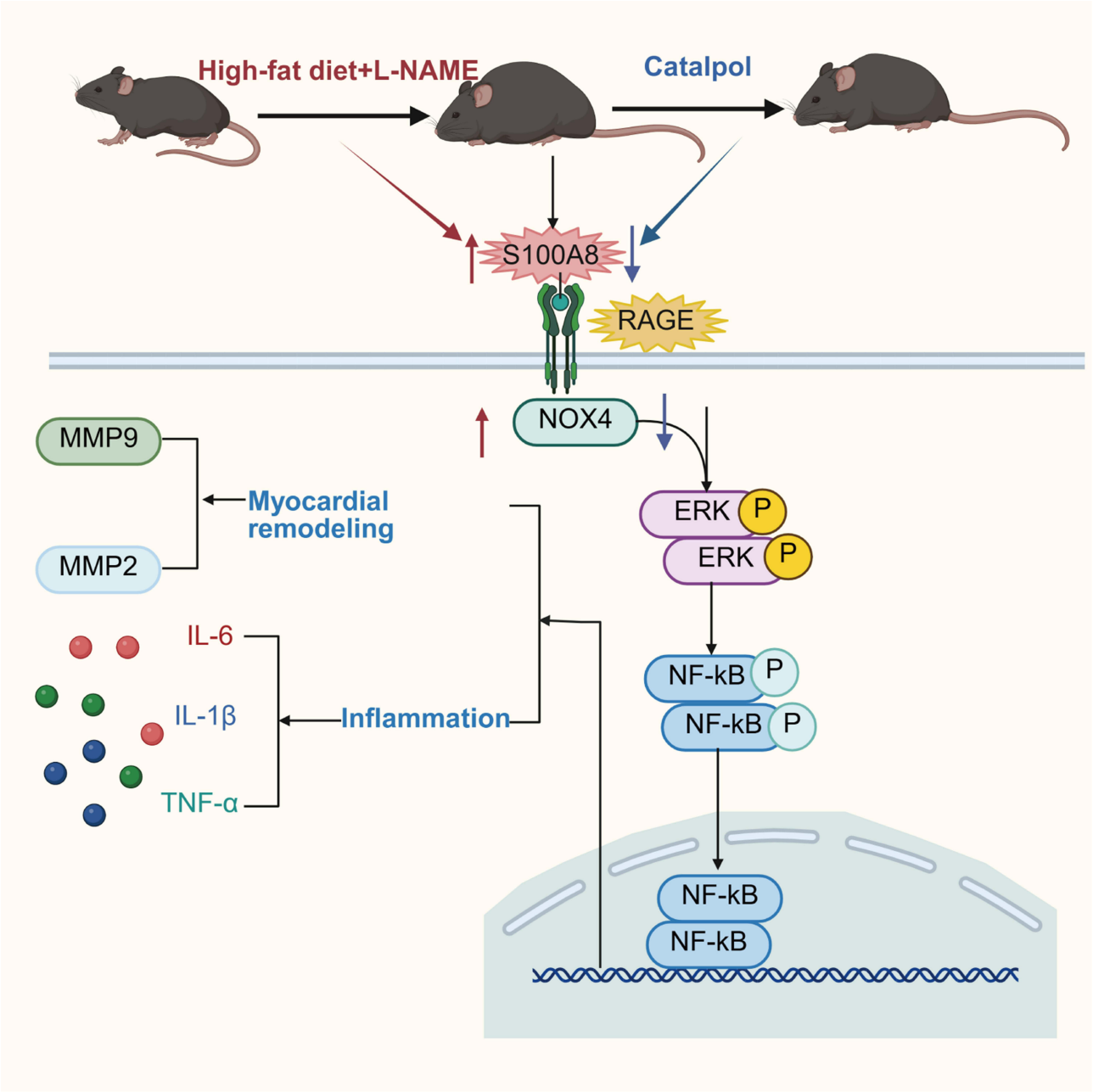

extracellular matrix (ECM) remodeling, which collectively contribute to myocardial stiffening and disease progression.[6,7] However, current therapeutic strategies remain largely empirical and symptom-oriented,[8,9] underscoring the urgent need to develop mechanism-based pharmacological interventions.

Catalpol (CAT), an iridoid glycoside primarily isolated from Rehmannia glutinosa, possesses the molecular formula $C_{15}H_{22}O_{10}$ and a characteristic iridoid cyclopentanoid monoterpene structure, including antioxidant, anti-inflammatory, and anti-apoptotic effects.[10–12] In various animal models, including ischemic cardiomyopathy, myocardial infarction, diabetic cardiomyopathy, and atherosclerosis, CAT has demonstrated remarkable cardioprotective effects.[13–16] In vitro studies further revealed that CAT significantly alleviates oxygen-glucose deprivation/reoxygenation (OGD/R)-induced

inflammation and myocardial injury in H9C2 cells.[17] Moreover, CAT regulates energy metabolism and inflammatory responses through activation of SIRT5-mediated signaling.[18] Additionally, CAT inhibits the production of key inflammatory mediators, including tumor necrosis factor-α (TNF-α), interleukin-6 (IL-6), and interleukin-1β (IL-1β), by suppressing the NF-κB signaling pathway.[19,20] Despite the well-documented cardioprotective effects of CAT, its specific therapeutic mechanisms and molecular targets in HFpEF remain to be fully elucidated.

Network pharmacology has emerged as a powerful approach for comprehensively mapping the interactions between traditional Chinese medicines and complex disease networks. Nevertheless, as a computational prediction paradigm, it requires rigorous experimental validation. Recent advances in multi-omics technologies, particularly transcriptomics, have enabled the identification of differentially expressed genes (DEGs), providing novel systems biology strategies to elucidate drug action mechanisms.

In this study, a mouse model of heart failure with preserved ejection fraction (HFpEF) was established using a high-fat diet (HFD) combined with Nω-nitro-L-arginine methyl ester (L-NAME), while an angiotensin II–induced H9C2 cell injury model was employed in vitro. To evaluate the therapeutic effects of CAT on HFpEF, we integrated network pharmacology and transcriptomic analyses to predict its potential mechanisms, which were subsequently validated through in vivo and in vitro experiments as well as molecular docking. Our findings aim to provide novel mechanistic insights and experimental evidence supporting CAT as a potential therapeutic candidate for HFpEF.

Materials and Methods

Chemicals and Materials

CAT (99.98% purity) was acquired from MedChemExpress (Shanghai, China). L-NAME was obtained from Sigma-Aldrich (Shanghai, China). Primary antibodies against the following targets were used: S100A8 (15792-1-AP), RAGE (16346-1-AP), NOX4 (14347-1-AP), MMP2 (10373-2-AP), and GAPDH (60004-1-AP) from Proteintech (Wuhan, China); ERK1/2 (9102), phospho-ERK1/2 (p-ERK1/2, 4370), p65 (8242), and phospho-p65 (p-p65, 3033) from Cell Signaling Technology (Danvers, MA, USA). Horseradish peroxidase-conjugated secondary antibodies were sourced from Zhongshan Goldenbridge Biotechnology (Beijing, China). Recombinant rat S100A8 protein with a His-tag (rS100A8, HY-P71275, MCE).

Animals and Therapy

Male C57BL/6 mice (25 g, mean weight) were purchased from Slack Laboratory Animal Co., Ltd. (Shanghai, China) and maintained under specific pathogen-free conditions (22–24 °C, 40–60% humidity, 12 h light/dark cycle) with ad libitum access to food and water. All animal experiments were conducted in accordance with the Guide for the Care and Use of Laboratory Animals (National Research Council, 8th edition, 2011) and were approved by the Animal Ethics Committee of Yueyang Hospital of Integrated Traditional Chinese and Western Medicine, Shanghai University of Traditional Chinese Medicine (Approval No. YYLAC-2024-262).

After a 7-day acclimation, 24 mice were randomly divided into three groups (n = 8 per group) using SPSS Statistics 27.0 (IBM Corp.; seed = 123,456): 1) Control group: standard chow and water; 2) Model group: high-fat diet (HFD, 60% kcal fat; Ready Bite® D12492i) and L-NAME (0.5 g/L, pH 7.4, Sigma#: N5751) in drinking water for 16 weeks; 3) CAT group: same HFD/L-NAME regimen with catalpol (CAT, 20 mg/kg, oral gavage) administered daily during weeks 13–16. The CAT dosage was selected based on established efficacy in previous studies.[14,21] Control and model mice received equal-volume saline. All animals were euthanized humanely by intraperitoneal injection of pentobarbital sodium (40 mg/kg, 2% solution).

Cell Culture and Treatment

H9C2 cells (iCell-r012, iCell Bioscience Inc.) were cultured in Dulbecco's Modified Eagle Medium (DMEM; iCell-128-0001, iCell Bioscience Inc.) supplemented with 10% fetal bovine serum (FBS; CY101, Epizyme Biotech) and 1% penicillin–streptomycin (15140122, Gibco). The cells were maintained in a humidified incubator at 37°C with 5% CO_2. For experimental procedures, cells were randomly assigned to five groups: (1) Control group: untreated cells; (2) Ang II

group: cells stimulated with 1 μmol/L angiotensin II (Ang II) for 24 h; (3) CAT group: cells treated with 40 μmol/L CAT following 24 h of Ang II stimulation; (4) rS100A8 group: cells treated with 1 μg/mL rS100A8 following 24 h of Ang II stimulation; (5) CAT + rS100A8 group: cells sequentially treated with 1 μg/mL rS100A8 and then 40 μmol/L CAT after 24 h of Ang II stimulation. All treatments were terminated 24 h after the initiation of the final treatment, and cells were collected for subsequent analyses. Each experiment was performed in triplicate and independently repeated three times to ensure reproducibility.

Cell Viability Assay

Cell viability was assessed using the Cell Counting Kit-8 (CCK-8; Bio-Rad). Cells were seeded in a 96-well plate at 6000 cells per well. After a 24 h pre-incubation, the cells were treated with various concentrations of CAT (2.5, 5, 10, 20, 40, 80, 160 μM) and rS100A8 (0.1, 0.2, 0.5, 1, 2, 5, 10 μg/mL) for 24 h. Following treatment, 10 μL of CCK-8 solution was added to each well, followed by a 2 h incubation. The absorbance was then measured at 450 nm using a microplate reader (Molecular Devices).

Echocardiography

Cardiac function was evaluated using a Vevo® 2100 imaging system (VisualSonics Inc., Toronto, Canada) equipped with a 40-MHz transducer. Mice were anesthetized with 1.5% (v/v) isoflurane in oxygen during imaging. Standard echocardiographic parameters were recorded, including LVEF and left ventricular fractional shortening (LVFS) from M-mode tracings. Early (E) and late (A) diastolic filling velocities were obtained by pulsed-wave Doppler, while early diastolic mitral annular velocity (e') was measured by tissue Doppler imaging. The E/A and E/e' ratios were subsequently calculated.

Oral Glucose Tolerance Test

After a 12-hour fast, mice received an oral glucose gavage (2 g/kg; Karan#: 50997). Blood glucose concentrations (mg/dL) were measured at baseline (0 min) and 15, 30, 60, 90, and 120 minutes after administration using a Contour TS glucometer (Bayer).

Blood Pressure Measurement

Systolic blood pressure (SBP) and diastolic blood pressure (DBP) were measured noninvasively using a tail-cuff system (BP-98E; Softron Biotechnology, China). Mice were acclimated in 37°C temperature-regulated cylindrical restrainers for ≥3 minutes before measurements. A minimum of five consecutive readings per mouse were recorded to determine SBP and DBP values.

Histological Analysis

Cardiac tissues were fixed in 4% paraformaldehyde, dehydrated, paraffin-embedded, and sectioned at 3–4 μm thickness. Morphology was assessed using hematoxylin-eosin (H&E) staining, while collagen deposition was analyzed via Masson's trichrome staining. All sections were imaged using a Nikon Eclipse Ci microscope equipped with a DS-Fi3 camera. Image analysis was performed using SlideViewer analysis software.

Rhodamine Phalloidin Staining

Cells grown on coverslips were fixed and permeabilized. Subsequently, F-actin was labeled by incubation with Phalloidin working solution (CA1620, Solarbio) for 2 hours in the dark, and nuclei were counterstained with DAPI (B0025, Bolfe) for 10 minutes. All staining steps were followed by three 5-minute washes with PBS. Finally, the coverslips were mounted and imaged using a fluorescence microscope.

Network Pharmacology

The chemical structure of CAT (PubChem CID: 91520) was retrieved from the PubChem database. Potential CAT targets were predicted using the pharmacological databases Traditional Chinese Medicine Systems Pharmacology (TCMSP),

SwissTargetPrediction, PharmMapper, and TargetNet. Genetic targets associated with HFpEF were retrieved from the disease databases GeneCards, Therapeutic Target Database (TTD), and Online Mendelian Inheritance in Man (OMIM) using the keyword "heart failure with preserved ejection fraction". Common targets between CAT and HFpEF were determined using Venny 2.1. A protein-protein interaction (PPI) network for the common targets was constructed using the STRING database (organism: Homo sapiens; confidence score ≥0.4; hidden unconnected nodes) and analyzed in Cytoscape (v3.10.2) to identify hub targets and visualize the compound–target–disease network. Functional enrichment of shared targets was performed by Gene Ontology (GO) and Kyoto Encyclopedia of Genes and Genomes (KEGG) analyses using the DAVID platform, and the results were visualized via the Bioinformatics online platform (http://www.bioinformatics.com.cn/).

Transcriptomics

Total RNA was extracted using TRIzol™ reagent (Thermo Fisher Scientific, USA). RNA integrity and concentration were evaluated with an Agilent 4200 Bioanalyzer and a Qubit fluorometer. Poly(A)+ mRNA was purified using oligo(dT) magnetic beads, and sequencing libraries were constructed with the TransNGS® Index Primers Kit. Raw reads generated on the Illumina platform were processed with fastp (v0.12.4) to remove adapters, poly-N sequences, and low-quality bases. Clean reads were aligned to the reference genome using STAR, and differentially expressed genes (DEGs) were identified with DESeq2 (v1.38.1) using $|\log_2(\text{fold change})| \geq 1$ and adjusted $p < 0.05$ as thresholds.

Molecular Docking

Molecular docking was performed to predict the interaction between CAT and its potential targets (S100A8, RAGE, NOX4, ERK1, and MMP2). Crystal structures of target proteins were obtained from the Protein Data Bank (https://www.rcsb.org/). After removing water molecules and co-crystallized ligands in PyMOL, hydrogen atoms were added using AutoDockTools (v1.5.7). The CAT structure was retrieved from PubChem, converted, and optimized for docking. Docking was conducted in AutoDock Vina, and the lowest-energy binding conformation was selected and visualized in PyMOL for interaction analysis.

Quantitative Real-Time PCR (qPCR)

Total RNA was using TRIzol reagent (Solarbio, Beijing, China). Complementary DNA synthesis was performed with a TransGen Biotech reverse transcription kit (AE311-03; Beijing, China). qPCR analysis was conducted on a SLAN-96P real-time PCR system (Hongshi Medical Technology, Shanghai, China) using ToloBio SYBR Green Master Mix (22204; Shanghai, China). GAPDH served as the endogenous reference gene. Relative gene expression was calculated using the 2^(-ΔΔCT) method. Primer sequences are provided in Table 1.

Western Blotting (WB)

WB was performed as previously described with minor modifications.[22] Protein bands were visualized using enhanced chemiluminescence substrate and imaged with a chemiluminescent imaging system.

Statistical Analysis

Multiple group comparisons employed one-way analysis of variance in GraphPad Prism 10. Results are expressed as mean ± standard deviation ($n \geq 3$). Statistical significance was defined as $p < 0.05$.

Results

CAT Ameliorated the Phenotype in HFpEF Mice

To assess CAT treatment efficacy, an HFpEF mouse model was established via combined HFD and L-NAME administration and then assessed phenotypic alterations (Figure 1A). The HFpEF mice demonstrated significant weight gain, impaired glucose tolerance, and altered SBP/DBP compared to controls. Subsequently, the efficacy of CAT in ameliorating HFpEF was evaluated. Relative to model controls, CAT-treated mice demonstrated marked body weight reduction

Table 1 The Primer Sequences for qPCR

Gene	Species	Forward (5′–3′)	Reverse (5′–3′)
TNF-α	Mouse	TAGCCCACGTCGTAGCAAAC	GCAGCCTTGTCCCTTGAAGA
IL-6	Mouse	GGGACTGATGCTGGTGACAA	TGCCATTGCACAACTCTTTTC
IL-1β	Mouse	ATGCCACCTTTTGACAG-TGATG	TGATGTGCTGCTGCGAGATT
Nppa	Mouse	CTGCTAGACCACCTGGAGGA	GGTACCGGAAGCTCACAGTC
BNP	Mouse	GAGGTCACTCCTATCCTCTGG	GCCATTTCCTCCGACTCTTT
GAPDH	Mouse	ACTCAGGAGAGTGTTTCCTCG	TGAAGGGGTCGTTGATGGC
IL-1β	H9C2	CAGCTTTCGACAGTGAGGAGA	TGTCGAGATGCTGCTGTGAG
IL-6	H9C2	ACAAGTCCGGAGAGGAGACT	TTGCCATTGCACAACTCTTTTC
TNF-α	H9C2	GATCGGTCCCAACAAGGAGG	CTTGGTGGTTTGCTACGACG
Nppa	H9C2	CTGATGGATTTCAAGAACCTGCT	CAGAGAGGGAGCTAAGTGCC
GAPDH	H9C2	TTCACCACCATGGAGAAGGC	CTCGTGGTTCACACCCATCA

Abbreviations: HFpEF, Heart failure with preserved ejection fraction; CAT, Catalpol; H&E, hematoxylin-eosin; WB, Western blotting; qPCR, quantitative real-time PCR; TNF, tumor necrosis factor; TCM, Traditional Chinese Medicine; TNF-α, tumor necrosis factor-alpha; IL-6, Interleukin-6; IL-1β, Interleukin-1beta; DEGs: differentially expressed genes; L-NAME: Nω-nitro-L-arginine methyl ester; HFD, high-fat diet; LVEF, left ventricular ejection fraction; LVFS, left ventricular fractional shortening; E, early diastolic transmitral flow velocity; A, late (atrial) diastolic transmitral flow velocity; e', early diastolic mitral annular velocity; SBP, systolic blood pressure; DBP, diastolic blood pressure; TCMSP, Traditional Chinese Medicine Systems Pharmacology; TTD, Therapeutic Target Database; OMIM, Online Mendelian Inheritance in Man; PPI, protein-protein interaction; BP, biological processes; CC, cellular components; MF, molecular functions; GO, Gene ontology; KEGG, Kyoto Encyclopedia of Genes and Genomes; ECM, extracellular matrix.

(Figure 1B) and enhanced glucose tolerance (Figure 1C), and markedly lowered SBP/DBP (Figure 1D and E). Representative echocardiographic images of the different groups after four weeks of intervention are shown in Figure 1F. No significant changes in LVEF or LVFS were observed across all groups through echocardiographic assessment (Figure 1G and H). HFpEF mice exhibited impaired diastolic function compared to controls, with pulse-wave Doppler showing significantly increased mitral early diastolic transmitral flow velocity/late (atrial) diastolic transmitral flow velocity (E/A) and early diastolic transmitral flow velocity/early diastolic mitral annular velocity (E/e') ratios. After the intervention of CAT, both parameters exhibited a significant reduction (Figure 1I and J), indicating that CAT markedly enhanced cardiac diastolic function. The expression of heart failure biomarkers ANP and BNP was markedly increased in HFpEF mice but significantly reduced by CAT treatment (Figure 1K and L). Disorganized myocardial architecture, inflammatory cell infiltration, and marked fibrosis were ob-served in model group via H&E and Masson's trichrome staining. These pathological features were significantly attenuated by CAT treatment in murine cardiac tissues (Figure 1M–O).

Network Pharmacology Revealed the Core Targets and Underlying Mechanisms of CAT in Treating HFpEF

Network pharmacology analysis was utilized to elucidate the biological mechanisms underlying the effects of CAT on HFpEF and to identify potential therapeutic targets. Through the databases of TCMSP, SwissTarget, PharmMapper and TargetNet, we identified 409 targets in CAT. Concurrently, 2443 HFpEF-associated targets were retrieved from TTD, OMIM, and GeneCards. 74 common targets were identified for CAT and HFpEF (Figure 2A). Subsequently, a PPI network comprising the common targets was developed utilizing the STRING database (Figure 2B). The network was constructed and topologically analyzed in Cytoscape, with the top 10 core targets subsequently identified, including GAPDH, CASP3, MMP9, BCL2, CTNNB1, GSK3B, LCAM1, HSP90AA1, ACE and MMP2 (Figure 2C). Using Cytoscape software, a "component-target-disease" network was constructed based on the common targets (Figure 2D).

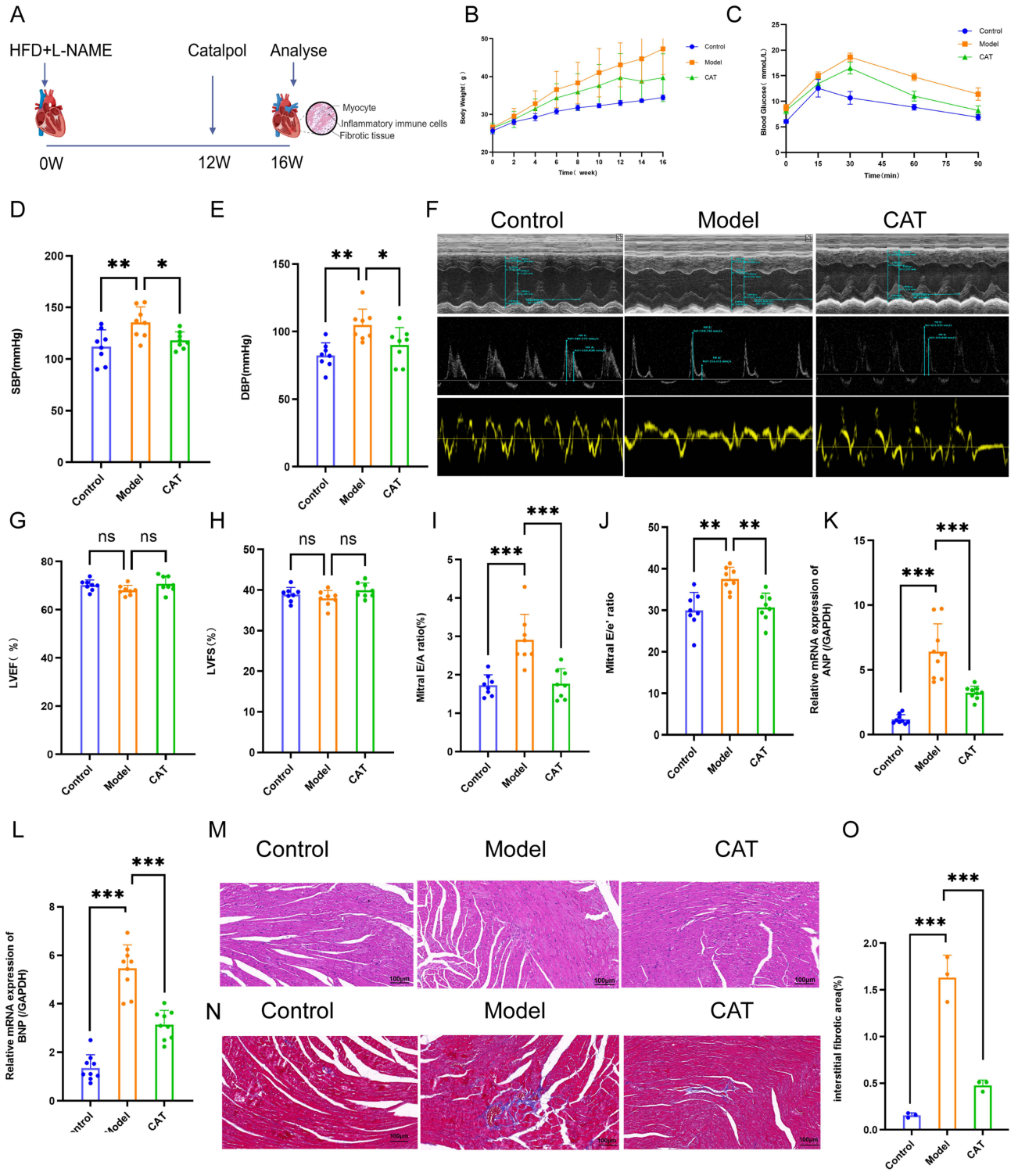

Figure 1 Effects of CAT on cardiac function and histology in vivo. (**A**) Schematic diagram of the experimental design. (**B**) Body weight of mice in each group (n = 8). (**C**) Glucose tolerance test after four weeks of intervention (n = 8). (**D**) SBP of each group (n = 8). (**E**) DBP of each group (n = 8). (**F**) Representative echocardiographic images after four weeks of intervention (n = 8), blue arrows indicate echocardiographic measurements of cardiac structural parameters (IVSd, IVSs, LVIDd, LVIDs, LVPWd, LVPWs, HR, E-wave, and A-wave). (**G–J**) Quantitative analysis of echocardiographic parameters (n = 8). (**K**) Nppa (ANP) mRNA expression (n = 3). (**L**) Nppb (BNP) mRNA expression (n = 3). (**M**) Representative H&E staining of cardiac tissue after four weeks of intervention (n = 3). (**N**) Representative Masson staining of cardiac tissue after four weeks of intervention (n = 3), the black line bar represents a 100 μm scale bar. (**O**) Quantification of the fibrotic area in cardiac tissue (n = 3). Data are presented as mean ± SD. *$p < 0.05$, **$p < 0.01$, ***$p < 0.001$.

Abbreviations: ns, not significant; SBP, Systolic blood pressure; DBP, Diastolic blood pressure.

https://doi.org/10.2147/JIR.S552741

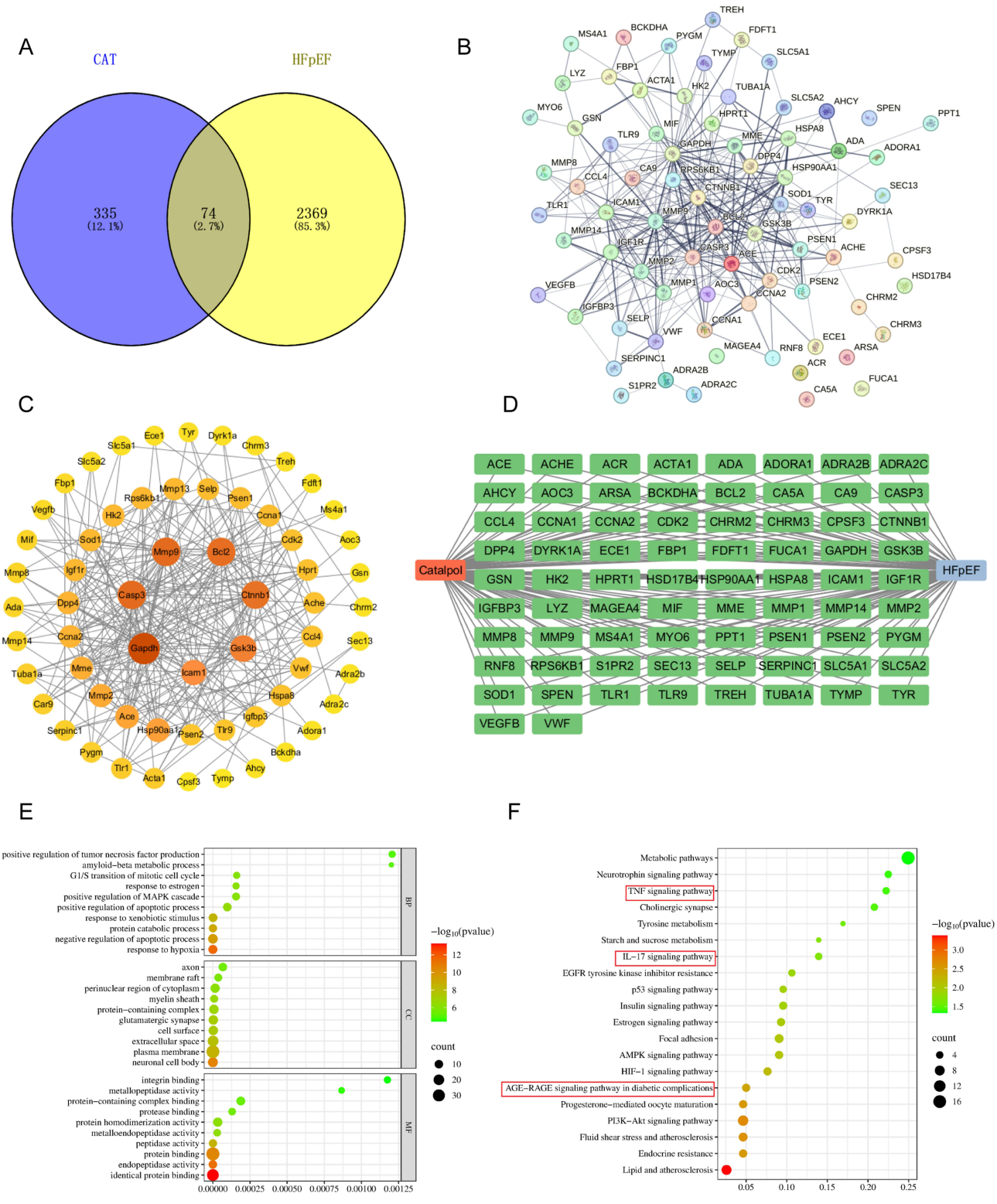

Figure 2 Network pharmacological analysis of the potential mechanisms of CAT in the treatment of HFpEF. (**A**) Venn diagram showing the overlapping targets of CAT and HFpEF. (**B**) PPI network diagram. (**C**) Visualization of key targets identified in the PPI network using Cytoscape software, where larger and redder nodes indicate higher degree values. (**D**) Compound–target–disease interaction network. (**E**) GO functional enrichment analysis of the top 10 pathways. (**F**) KEGG pathway enrichment analysis of the top 20 pathways. The red rectangular box indicates the key pathways of interest in this study.

Functional enrichment analysis of common targets was conducted in DAVID, including GO biological processes and KEGG pathway mapping, to characterize underlying molecular mechanisms. Significant results were organized according to the magnitude of the P value. GO categorization demonstrated significant enrichment of common targets in: (1) biological processes (BP): including TNF response and hypoxia adaptation; (2) cellular components (CC): predominantly localized to the plasma membrane and cell surface; (3) molecular functions (MF): protein-containing complex and protein phosphatase binding (Figure 2E). KEGG pathway enrichment analysis identified significant signaling pathways, including the RAGE pathway (Figure 2F).

Transcriptomics Predicted Key Biological Processes and Pathways of CAT in Treating HFpEF

To elucidate CAT's therapeutic mechanism in HFpEF, we subsequently performed transcriptome sequencing on cardiac tissues. The results of principal component analysis revealed notable differences between control and model group, validating successful disease modeling (Figure 3A). Transcriptomics identified 160 DEGs in model versus control group. Among these, 68 genes were found to be up-regulated, while 92 genes exhibited down-regulation (Figure 3B). There are 390 differentially abundant transcripts between CAT and model groups, comprising 116 upregulated and 274 down-regulated genes (Figure 3C). The heat map of cluster analysis of DEGs is shown in the Figure 3D and E. Notably, in the model group, genes like S100a8 and NOX4 were significantly upregulated, while in the CAT group, these genes showed a significant downregulation (Figure 3F).

Subsequent KEGG pathway and GO functional enrichment analyses were per-formed on the 386 DEGs identified in CAT versus model comparisons. GO functional enrichment analysis shows that BP mainly involve responses to biological stimuli and immune responses, etc.; CC mainly include extracellular regions, cell surfaces, etc.; and MF mainly include enzyme binding and signaling receptor binding, etc. Enrichment bubble diagrams were constructed for the twenty most statistically significant path-ways (P-value ranked), which included key inflammatory response pathways like the TNF and RAGE signaling pathways (Figure 3G). Additionally, visual mapping of the RAGE signaling pathway was performed via KEGG Mapper tool (https://www.genome.jp/kegg/mapper/) (Figure 3H).

Molecular Docking Analysis

Molecular docking was executed to assess binding affinities between CAT and core components (S100a8, RAGE, NOX4) of the target pathway. The crystal structures of S100a8 (PDB: 1xk4), ERK1 (PDB: 2zoq), MMP2 (PDB: 8h78), NOX4 (PDB: 4ut2), and RAGE (PDB: 3o3u) were retrieved from the PDB, and docked using AutoDock Vina to predict optimal ligand-receptor binding sites and binding affinities. Notably, lower binding energy indicates higher affinity. The binding energies of CAT with S100a8 (Figure 4A), RAGE (Figure 4B), NOX4 (Figure 4C), ERK1 (Figure 4D), and MMP2 (Figure 4E) were −7.5, −7.4, −7.5, −6.6, and −6.2 kcal/mol, respectively.

The Effect of CAT on the S100a8/RAGE/NOX4 Signaling Pathway

Integrated network pharmacology, transcriptomic, and molecular docking analyses identified the S100a8/RAGE/NOX4 signaling axis as closely associated with HFpEF pathogenesis. To further elucidate the mechanism of CAT on HFpEF, protein expression levels of S100a8, RAGE, NOX4, ERK1/2, p65, MMP2, along with the phosphorylation status of ERK1/2 (p-ERK1/2) and p65 (p-p65), were quantified in murine cardiac tissue (Figure 5A and Supplementary Figure 1). WB analysis demonstrated significantly elevated expression of S100a8, RAGE, NOX4, ERK1/2, p-ERK1/2, p65, p-p65, and MMP2 in the model group versus controls. Crucially, CAT administration markedly downregulated the expression of proteins within the S100a8/RAGE/NOX4 signaling axis and its downstream effector, MMP2 (Figure 5B–G).

To assess the impact of CAT on cardiac inflammation in HFpEF mice, mRNA levels of key pro-inflammatory cytokines (TNF-α, IL-6, IL-1β) downstream of the S100a8/RAGE/NOX4 axis were quantified via qPCR. Compared to the control group, the model group exhibited significantly elevated mRNA levels of TNF-α, IL-6, and IL-1β. Notably, CAT treatment substantially reduced the expression of these inflammatory mediators (Figure 5H–J). In summary, these

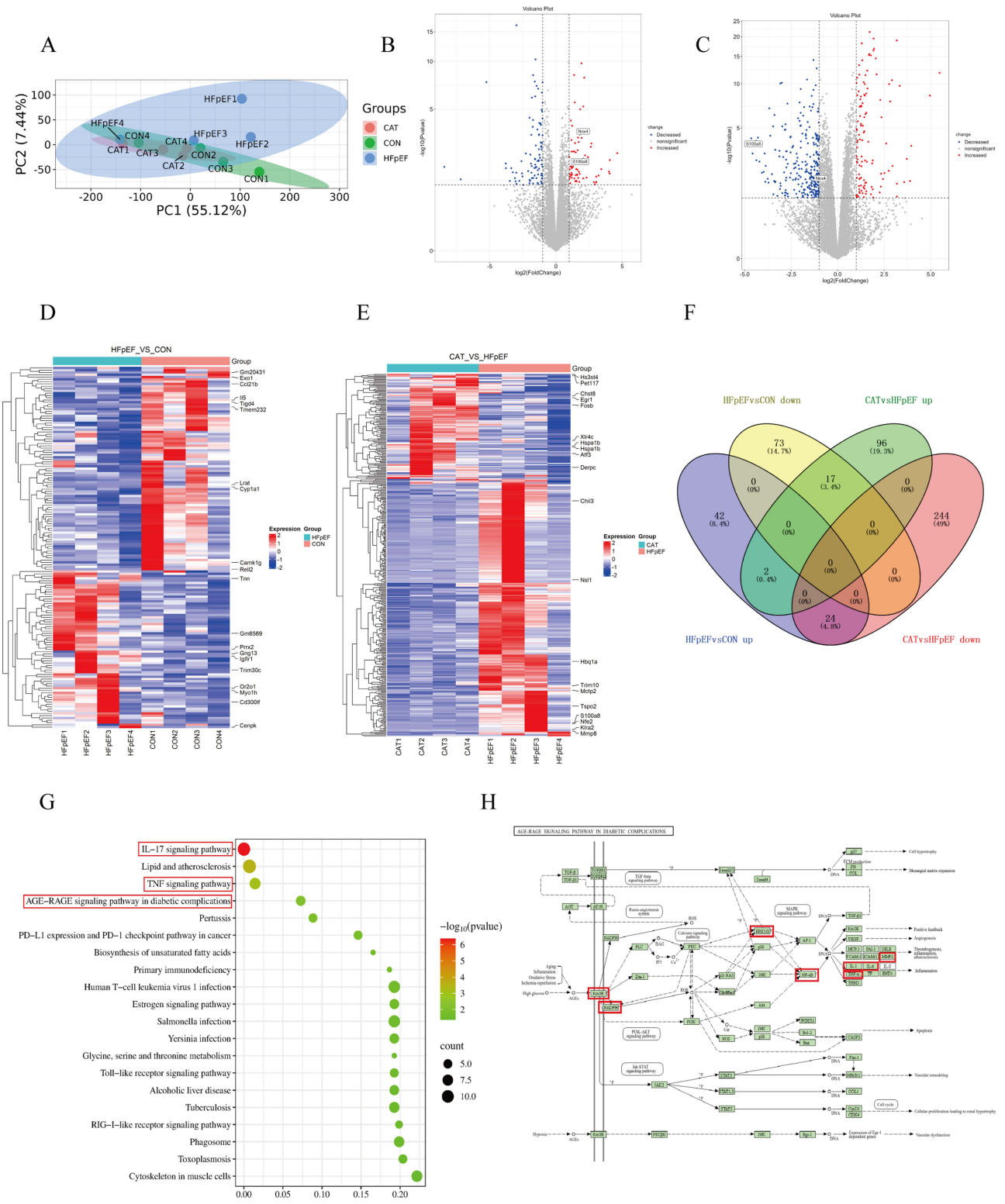

Figure 3 Transcriptomic analysis of CAT in the treatment of HFpEF in mice. (**A**) PCA of DEGs across Control, HFpEF, and CAT groups. (**B**) Volcano plot of DEGs between Control and HFpEF groups. (**C**) Volcano plot of DEGs between HFpEF and CAT groups. (**D**) Heatmap of DEGs between Control and HFpEF groups. (**E**) Heatmap of DEGs between HFpEF and CAT groups. (**F**) Venn diagram of DEGs among the three groups. (**G**) KEGG pathway enrichment analysis of DEGs between HFpEF and CAT groups. The red box indicates the key pathways related to this study. (**H**) KEGG signaling pathways for RAGE. The red box marks the key targets in the RAGE signaling pathway.

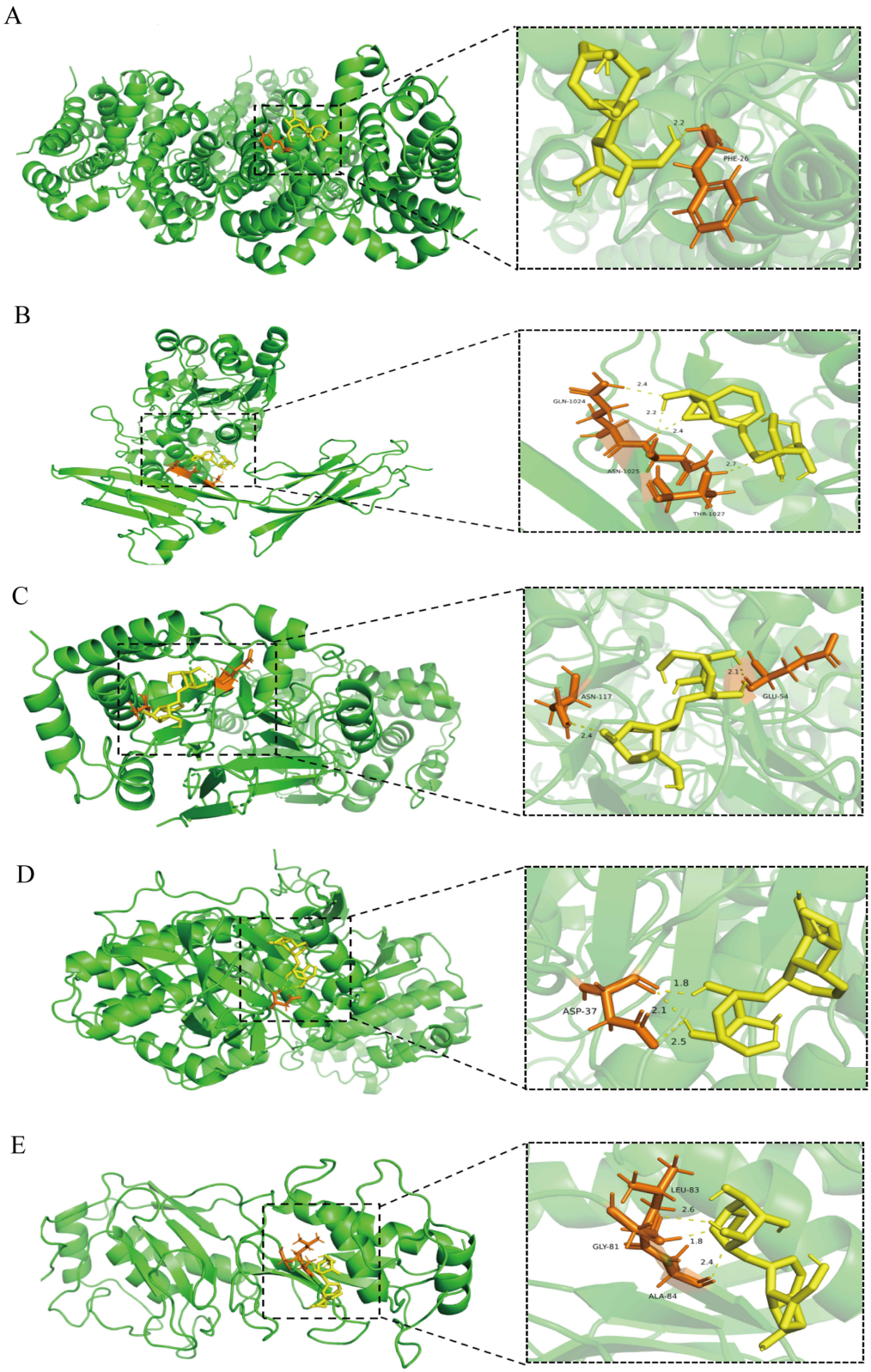

Figure 4 Visualization of molecular docking results using interaction diagrams. (**A**) Molecular docking of CAT and ERK1. (**B**) Molecular docking of CAT and MMP2. (**C**) Molecular docking of CAT and NOX4. (**D**) Molecular docking of CAT and RAGE. (**E**) Molecular docking of CAT and S100A8.

https://doi.org/10.2147/JIR.S552741

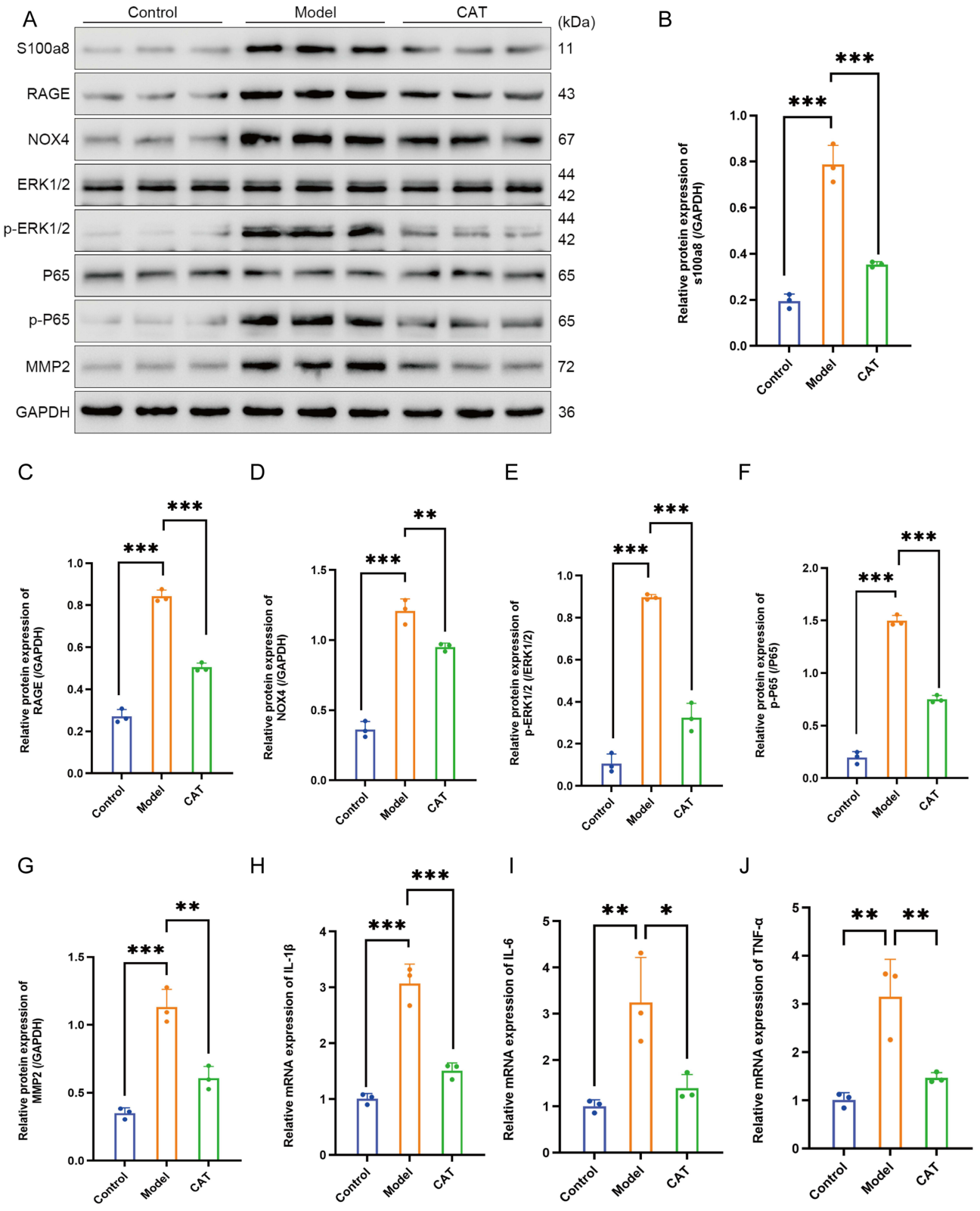

Figure 5 CAT downregulated the S100A8-RAGE-NOX4 signaling pathway in HFpEF. (**A**) Representative WB bands of S100A8, RAGE, NOX4, ERK, p-ERK, P65, p-P65, and MMP2. (**B**–**G**) Quantification of protein expression levels analyzed using ImageJ software (n=3). (**H**) Quantitative analysis of IL-1β expression (n=3). (**I**) Quantitative analysis of IL-6 expression (n=3). (**J**) Quantitative analysis of TNF-α expression (n=3). Data are presented as mean ± SD. *$p < 0.05$, **$p < 0.01$, ***$p < 0.001$.

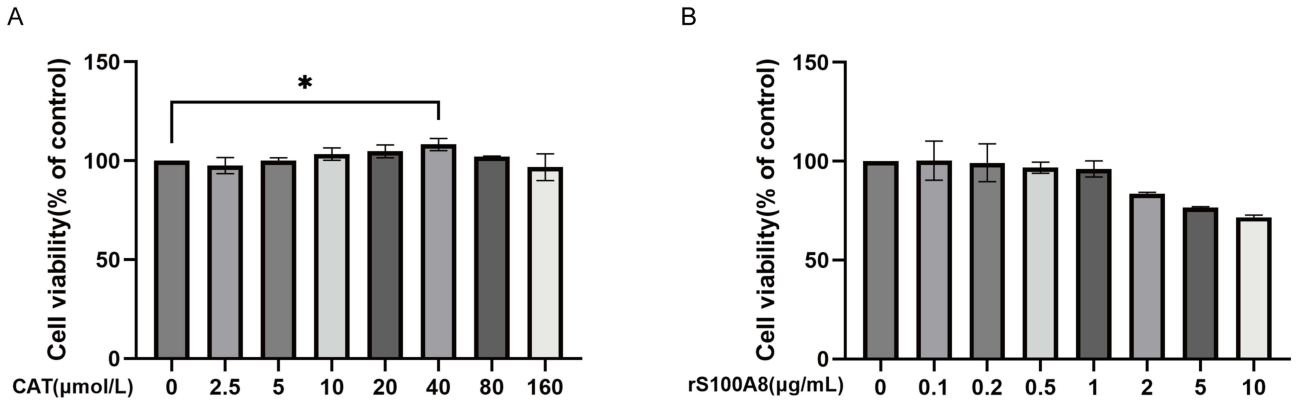

Figure 6 Effects of CAT and rS100A8 on the viability of H9C2 cardiomyocytes. (**A**) Cell viability of H9C2 cells treated with various concentrations of CAT for 24 h was determined by the CCK-8 assay (n = 3). (**B**) Effects of rS100A8 on H9C2 cell viability were evaluated by the CCK-8 assay (n = 3). Data are presented as mean ± SD. *$p < 0.05$.

findings suggest that CAT may improve HFpEF in mice by downregulating the expression of proteins within the S100a8/RAGE/NOX4 signaling axis and reducing the levels of inflammatory factors.

Screening of Optimal Concentrations for CAT and rS100A8 in vitro

Cell viability assays revealed that most concentrations of CAT had no significant effect on H9C2 cell viability compared with the control group, whereas 40 μmol/L CAT significantly promoted cell proliferation (Figure 6A). Therefore, 40 μmol/L was selected as the treatment concentration for subsequent in vitro experiments. H9C2 cells were treated with rS100A8 at different concentrations (0.1, 0.2, 0.5, 1, 2, 5, and 10 μg/mL) for 24 h. The results showed that 1 μg/mL rS100A8 did not significantly affect cell viability compared with the control, whereas higher concentrations led to a gradual decline (Figure 6B). Thus, 1 μg/mL was selected as the optimal in vitro concentration of rS100A8.

CAT Attenuates Ang II–Induced Inflammatory Response in H9C2 Cells by Downregulation the S100a8/RAGE/NOX4 Signaling Axis

Based on in vivo findings, CAT was shown to alleviate HFpEF-induced inflammation by downregulating the S100a8/RAGE/NOX4 signaling axis. To further verify the anti-inflammatory effects of CAT in the treatment of HFpEF, an in vitro model was established by treating H9C2 cells with Ang II. To evaluate the therapeutic effects of CAT on H9C2 cells, cell morphology was first examined using phalloidin staining, and the mRNA expression levels of inflammation-related genes were measured. As shown in Figure 7A and B, Ang II treatment markedly increased the cross-sectional area of H9C2 cells compared with the control group, while the addition of rS100A8 further exacerbated this pathological hypertrophy. In contrast, CAT intervention can effectively alleviate cell hypertrophy induced by Ang II or Ang II + rS100A8. At the molecular level, Ang II stimulation significantly upregulated the mRNA expression of heart failure and inflammation markers, including ANP, IL-1β, IL-6, and TNF-α. Similarly, rS100A8 addition further amplified the pro-inflammatory effects of Ang II, whereas CAT treatment markedly suppressed the overexpression of these genes (Figure 7C–F).

To elucidate the molecular mechanism underlying the anti-inflammatory effects of CAT, WB analysis was performed to examine the expression of key proteins in the S100a8/RAGE/NOX4 signaling axis. As shown in Figure 7G–J and Supplementary Figure 2, Ang II treatment markedly increased the protein levels of S100A8, its receptor RAGE, and the downstream effector NOX4 in H9C2 cardiomyocytes. Notably, CAT administration significantly suppressed the expression of all three key proteins. In addition, the presence of rS100A8 attenuated the inhibitory effects of CAT, indicating that activation of the S100A8/RAGE pathway partially counteracted CAT's protective action.

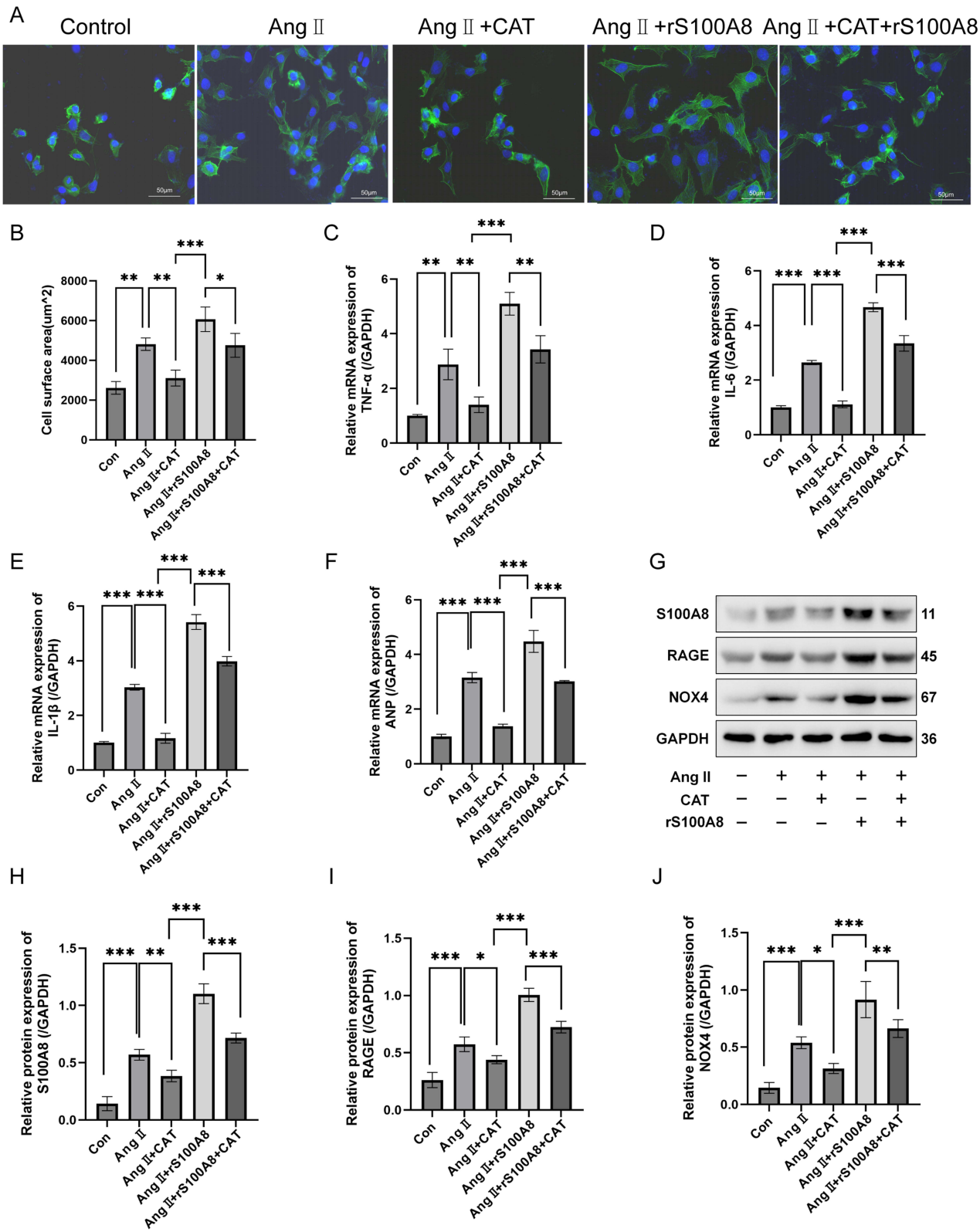

Figure 7 Effects of CAT on Angiotensin II–Induced H9C2 Cells in vitro. (**A**) Representative phalloidin staining images. Scale bar, 50 μm. (**B**) Quantification of cell surface area (n = 3). (**C**–**E**) Relative mRNA expression levels of proinflammatory cytokines TNF-α, IL-6, and IL-1β determined by qPCR (n = 3).(**F**) Relative mRNA expression of the hypertrophic marker Nppa (ANP) (n = 3). (**G**) Representative Western blot images of related proteins (n = 3). (**H**–**J**) Quantitative analysis of protein expression levels (n = 3). Data are presented as mean ± SD. **p* < 0.05, ***p* < 0.01, ****p* < 0.001.

In summary, these in vitro results indicate that CAT can attenuate pathological hypertrophy of cardiomyocytes and suppress inflammatory responses, with its protective effects mediated through the downregulation of the S100a8/RAGE/NOX4 signaling pathway.

Discussion

HFpEF accounts for nearly 50% of all heart failure cases and is associated with a substantial burden of morbidity and mortality.[2] Inflammation contributes substantially to HFpEF pathogenesis by promoting cardiac remodeling, diastolic dysfunction, and reduced cardiac output.[6] TCM is widely employed in HFpEF management owing to its notable efficacy and favorable safety profile.[23–25]Substantial evidence indicates that CAT has a beneficial effect in preventing or treating cardiovascular diseases.[26–28] Pharmacokinetic studies have shown that oral CAT is rapidly absorbed. Using liquid chromatography-tandem mass spectrometry, it was reported that after oral administration of a 50 mg/kg dose of CAT, the half-life was approximately 1.2 hours, the time to peak concentration was about 1.3 hours.[29] Similar results were observed at higher doses (50 to 200 mg/kg), characterized by rapid absorption of CAT; however, the plasma concentrations increased in a less than proportional manner, indicating non-linear pharmacokinetics. At a dose of 50 mg/kg, the absolute bioavailability was found to be 66.7%,[30] supporting its potential for oral administration. CAT also exhibits extensive tissue distribution, with high levels detected particularly in the kidneys, liver, and heart, indicating its ability to reach cardiac tissue and exert pharmacological effects.[31] To improve CAT's stability and systemic exposure, lipid nanoparticle formulations have been developed, achieving encapsulation efficiencies of approximately 77% along with favorable stability profiles.[32] In this study, we per-formed a preliminary assessment of the therapeutic efficacy of CAT in HFpEF. Complementary approaches, including network pharmacology, transcriptomic analysis, and molecular docking, were integrated to delineate the underlying mechanisms; these predictions were further validated through in vitro and in vivo experimentation.

This study integrated network pharmacology, transcriptomic analysis, and experimental validation to systematically elucidate the potential mechanisms by which CAT ameliorates HFpEF. First, network pharmacology identified 74 potential targets of CAT against HFpEF, suggesting its multitarget pharmacological characteristics. However, these predicted targets required further refinement and confirmation through objective in vivo data. Subsequently, transcriptome sequencing of cardiac tissues from the HFpEF model revealed that the expression levels of S100A8 and NOX4 were among the most profoundly altered under disease conditions and were markedly reversed following CAT treatment. Furthermore, KEGG pathway enrichment analysis demonstrated that the RAGE signaling pathway was significantly enriched based on both the predicted targets and the differentially expressed genes, indicating a strong mechanistic convergence. Notably, S100A8 serves as a key ligand that activates the RAGE receptor,[33,34] while NOX4 functions as an important downstream effector mediating oxidative stress within the RAGE signaling pathway.[35] Collectively, these findings highlight the central role of the S100A8/RAGE/NOX4 axis in the pathogenesis of HFpEF and in the therapeutic effects of CAT. Therefore, our subsequent experiments were designed to further validate this signaling pathway through indepth mechanistic studies.

S100A8 is actively released during the inflammatory process.[36] Under pathological stress, S100A8 binding to RAGE initiates inflammatory pathway activation, inducing release of key pro-inflammatory mediators (notably TNF-α, IL-6, and IL-1β) that amplify inflammation.[37] Moreover, S100A8 potently induces fibroblast proliferation and differentiation into fibrosis-promoting myofibroblasts, consequently driving dysregulated ECM deposition.[38] RAGE has emerged as a key mediator of cardiac remodeling and heart failure progression. Activation of RAGE induces oxidative stress, inflammation, and autophagy dysregulation, thereby promoting myocardial fibrosis and dysfunction. Experimental studies show that RAGE deficiency or inhibition mitigates cardiac fibrosis by suppressing autophagy-dependent macrophage alternative activation and endothelial-to-mesenchymal transition (EndMT).[39,40] In pressure overload–induced models, RAGE blockade prevents excessive autophagy and preserves cardiac function.[41] Clinically, elevated circulating AGEs and RAGE gene polymorphisms are associated with poor outcomes in heart failure.[42–44] These findings suggest that RAGE drives adverse cardiac remodeling through autophagy- and inflammation-related mechanisms and represents a potential therapeutic target for cardiac protection. RAGE can interact with a variety of endogenous ligands, such as binding to NOX4, which can alleviate oxidative stress and inflammation.[45,46] NOX4 critically contributes to cardiovascular

pathobiology and emerges as a viable pharmacological target.[47] Cardiac-specific NOX4 overexpression in-duces fibrosis and hypertrophy, while its knockout attenuates these pathologies. Mechanistically, NOX4 drives fibroblast activation and collagen deposition via ERK signaling,[48] and in addition, it can aggravate the inflammatory response.[49] ERK phosphorylation triggers NF-κB nuclear translocation, upregulating proinflammatory cytokines (such as TNF-α and IL-1β),[50] promoting ECM protein synthesis (such as fibronectin and collagen),[51] and ultimately triggering inflammation and fibrosis. MMP2 and MMP9, key regulators of cardiomyocyte ECM metabolism, critically drive myocardial fibrosis and pathological structural remodeling via dysregulated collagen degradation and turnover. These enzymes significantly exacerbate the pathological progression of HFpEF.[52,53]

Collectively, our data support a mechanistic model wherein S100A8 binding to RAGE activates the NOX4-ERK-NF-κB signaling cascade. This activation promotes the release of pro-inflammatory mediators and ECM deposition, thereby contributing to HFpEF pathogenesis. Additionally, previous studies have also established that CAT exerts inhibitory effects on NF-κB activation, consequently attenuating the generation of pro-inflammatory cytokines, notably TNF-α, IL-6 and IL-1β.[54,55] Consistent with this, our in vitro and in vivo results indicate that CAT's therapeutic effects may involve suppression of key signaling molecules (S100A8, RAGE, NOX4, MMP2, ERK, NF-κB, and their phosphorylated counterparts) and reduction of pro-inflammatory cytokine mRNA.

Mechanistically, CAT exerts its therapeutic effects through a hierarchical and integrated process. First, molecular docking and rS100A8 rescue experiments suggest that CAT binds directly and with high affinity to the upstream alarmin S100A8, thereby inhibiting its biological activity and blocking the initiation of inflammatory signaling. Second, this upstream inhibition propagates through the signaling network, leading to reduced phosphorylation and activation of downstream mediators such as ERK1/2 and NF-κB. Consequently, by attenuating the activity of the central transcription factor NF-κB, CAT suppresses its dependent transcriptional output. This direct transcriptional inhibition leads to the downregulation of key downstream effectors, including NOX4 and MMP2, at both mRNA and protein levels.

This study has certain limitations. First, although the HFpEF model induced by a high-fat diet and L-NAME replicates several major features of human HFpEF, it cannot fully capture the heterogeneity and multifactorial nature of the clinical condition. Second, mechanistic experiments were mainly performed in H9C2 cardiomyoblasts. Given the heart's multicellular composition, particularly the critical role of cardiac fibroblasts in inflammation and fibrosis, it remains unclear whether CAT exerts similar protective effects via the S100A8–RAGE–NOX4 axis in fibroblasts. Future studies using primary cardiomyocytes and fibroblasts are warranted to clarify cell type–specific mechanisms of CAT's cardioprotection.Third, specific pharmacological inhibitors or gene-silencing approaches targeting S100A8 or RAGE were not utilized in this study to further verify the causal role of the S100A8/RAGE/NOX4 axis in mediating CAT's effects. Finally, all experiments were preclinical, whether CAT provides comparable benefits in human HFpEF requires further clinical investigation.

Conclusion

Our study demonstrates that CAT effectively ameliorates multiple pathological and functional abnormalities in HFpEF mice, including obesity, glucose intolerance, hypertension, diastolic dysfunction, myocardial inflammatory infiltration, and fibrosis. Integrated network pharmacology and transcriptomic analyses identified the RAGE signaling pathway as a key target of CAT, and molecular docking confirmed strong binding affinity of CAT with S100A8, RAGE, NOX4, ERK1, and MMP2. WB further validated that CAT significantly downregulates the S100A8/RAGE/NOX4 axis and its downstream effector MMP2 in cardiac tissue, consistent with the predicted results. In vitro, CAT attenuated Ang II–induced H9c2 cardiomyocyte hypertrophy, suppressed inflammatory cytokines (TNF-α, IL-1β, IL-6) and the HF marker ANP, and downregulated S100A8, RAGE, and NOX4, recapitulating the in vivo molecular effects. Importantly, activation of the pathway by recombinant S100A8 markedly diminished CAT's protective effects. Collectively, these findings indicate that CAT mitigates HFpEF by modulating the S100A8/RAGE/NOX4 signaling axis and its downstream targets, thereby reducing myocardial inflammation and fibrosis.

Acknowledgments

During the preparation of this manuscript, the author used BioRender for the purposes of graphics. The authors have reviewed and edited the output and take full responsibility for the content of this publication.

Author Contributions

All authors made a significant contribution to the work reported, whether that is in the conception, study design, execution, acquisition of data, analysis and interpretation, or in all these areas; took part in drafting, revising or critically reviewing the article; gave final approval of the version to be published; have agreed on the journal to which the article has been submitted; and agree to be accountable for all aspects of the work.

Funding

This work was supported by the National Natural Science Foundation of China (82474458), Yueyang Hospital of Integrated Traditional Chinese and Western Medicine, Shanghai University of Traditional Chinese Medicine Hospital-level Projects (2024yyzh03, 2024yyzh01).

Disclosure

The authors declare no conflicts of interest. The funders had no role in the design of the study; in the collection, analyses, or interpretation of data; in the writing of the manuscript; or in the decision to publish the results. All animal experiments were conducted in accordance with the Guide for the Care and Use of Laboratory Animals (National Research Council, 8th edition, 2011) and were approved by the Animal Ethics Committee of Yueyang Hospital of Integrated Traditional Chinese and Western Medicine, Shanghai University of Traditional Chinese Medicine (protocol code YYLAC-2024-262 and date of approval: 2024.8.12).

References

1. Pepin ME, Konrad PJM, Nazir S, et al. Mitochondrial NNT promotes diastolic dysfunction in cardiometabolic HFpEF. *Circ Res*. 2025;136(12):1564–1578. doi:10.1161/circresaha.125.326154
2. Redfield MM, Borlaug BA. Heart failure with preserved ejection fraction: a review. *JAMA*. 2023;329(10):827–838. doi:10.1001/jama.2023.2020
3. Hamo CE, DeJong C, Hartshorne-Evans N, et al. Heart failure with preserved ejection fraction. *Nat Rev Dis Primers*. 2024;10(1):55. doi:10.1038/s41572-024-00540-y
4. Shah SJ, Borlaug BA, Kitzman DW, et al. Research priorities for heart failure with preserved ejection fraction: national heart, lung, and blood institute working group summary. *Circulation*. 2020;141(12):1001–1026. doi:10.1161/circulationaha.119.041886
5. Zhang Z, Wang Y, Chen X, et al. The aging heart in focus: the advanced understanding of heart failure with preserved ejection fraction. *Ageing Res Rev*. 2024;101:102542. doi:10.1016/j.arr.2024.102542
6. Liu H, Magaye R, Kaye DM, Wang BH. Heart failure with preserved ejection fraction: the role of inflammation. *Eur J Pharmacol*. 2024;980:176858. doi:10.1016/j.ejphar.2024.176858
7. Paulus WJ, Tschöpe C. A novel paradigm for heart failure with preserved ejection fraction: comorbidities drive myocardial dysfunction and remodeling through coronary microvascular endothelial inflammation. *J Am Coll Cardiol*. 2013;62(4):263–271. doi:10.1016/j.jacc.2013.02.092
8. McDonagh TA, Metra M, Adamo M, et al. 2021 ESC guidelines for the diagnosis and treatment of acute and chronic heart failure. *Eur Heart J*. 2021;42(36):3599–3726. doi:10.1093/eurheartj/ehab368
9. Heidenreich PA, Bozkurt B, Aguilar D, et al. 2022 AHA/ACC/HFSA guideline for the management of heart failure: a report of the American College of Cardiology/American heart association joint committee on clinical practice guidelines. *J Am Coll Cardiol*. 2022;79(17):e263–e421. doi:10.1016/j.jacc.2021.12.012
10. Liu J, Liu S, Yu M, et al. Anti-inflammatory effect and mechanism of catalpol in various inflammatory diseases. *Drug Dev Res*. 2023;84(7):1376–1394. doi:10.1002/ddr.22096
11. Hassan MM, Fahmy MI, Azzam HN, Ebrahim YM, El-Shiekh RA, Aboulmagd YM. Multifaceted therapeutic potentials of catalpol, an iridoid glycoside: an updated comprehensive review. *Inflammopharmacology*. 2025. doi:10.1007/s10787-025-01694-1
12. Yang C, Shi Z, You L, Du Y, Ni J, Yan D. Neuroprotective effect of catalpol via anti-oxidative, anti-inflammatory, and anti-apoptotic mechanisms. *Front Pharmacol*. 2020;11:690. doi:10.3389/fphar.2020.00690
13. Zou G, Zhong W, Wu F, Wang X, Liu L. Catalpol attenuates cardiomyocyte apoptosis in diabetic cardiomyopathy via Neat1/miR-140-5p/HDAC4 axis. *Biochimie*. 2019;165:90–99. doi:10.1016/j.biochi.2019.05.005
14. Chen Q, Qi X, Zhang W, et al. Catalpol inhibits macrophage polarization and prevents postmenopausal atherosclerosis through regulating estrogen receptor alpha. *Front Pharmacol*. 2021;12:655081. doi:10.3389/fphar.2021.655081
15. Ge H, Lin W, Lou Z, et al. Catalpol alleviates myocardial ischemia reperfusion injury by activating the Nrf2/HO-1 signaling pathway. *Microvasc Res*. 2022;140:104302. doi:10.1016/j.mvr.2021.104302
16. Ju X, Xue D, Wang T, Ge B, Zhang Y, Li Z. Catalpol promotes the survival and VEGF secretion of bone marrow-derived stem cells and their role in myocardial repair after myocardial infarction in rats. *Cardiovasc Toxicol*. 2018;18(5):471–481. doi:10.1007/s12012-018-9460-4

17. Wang T, Shao C, An H, Xu G, Wan H, Yang J. Catalpol research on the mechanism of antimyocardial reperfusion injury by regulating the MiR-126/TWEAK-FN14 pathway: in vitro and computer simulation studies. *ACS Omega*. 2025;10(19):19538–19551. doi:10.1021/acsomega.4c11357
18. Huang C, Cui Y, Ji L, et al. Catalpol decreases peroxynitrite formation and consequently exerts cardioprotective effects against ischemia/reperfusion insult. *Pharm Biol*. 2013;51(4):463–473. doi:10.3109/13880209.2012.740052
19. Zaaba NE, Al-Salam S, Beegam S, Elzaki O, Yasin J, Nemmar A. catalpol attenuates oxidative stress and inflammation via mechanisms involving sirtuin-1 activation and NF-κB inhibition in experimentally-induced chronic kidney disease. *Nutrients*. 2023;15(1):237. doi:10.3390/nu15010237
20. Gao F, He Q, Wu S, et al. Catalpol ameliorates LPS-induced inflammatory response by activating AMPK/mTOR signaling pathway in rat intestinal epithelial cells. *Eur J Pharmacol*. 2023;960:176125. doi:10.1016/j.ejphar.2023.176125
21. Wu X, Zhang Y, Wang J, et al. Role of SIRT1-mediated synaptic plasticity and neurogenesis: sex-differences in antidepressant-like efficacy of catalpol. *Phytomedicine*. 2024;135:156120. doi:10.1016/j.phymed.2024.156120
22. Schiattarella GG, Altamirano F, Tong D, et al. Nitrosative stress drives heart failure with preserved ejection fraction. *Nature*. 2019;568(7752):351–356. doi:10.1038/s41586-019-1100-z
23. Kang Z, Wu Y, Ding Y, et al. Investigation of the efficacy of Dengzhan Shengmai capsule against heart failure with preserved ejection fraction. *J Ethnopharmacol*. 2024;333:118419. doi:10.1016/j.jep.2024.118419
24. Huang Y, Zhang K, Liu M, et al. An herbal preparation ameliorates heart failure with preserved ejection fraction by alleviating microvascular endothelial inflammation and activating NO-cGMP-PKG pathway. *Phytomedicine*. 2021;91:153633. doi:10.1016/j.phymed.2021.153633
25. Shi Y, Liu C, Xiong S, et al. Ling-Gui-Qi-Hua formula alleviates left ventricular myocardial fibrosis in rats with heart failure with preserved ejection fraction by blocking the transforming growth factor-β1 /Smads signaling pathway. *J Ethnopharmacol*. 2023;317:116849. doi:10.1016/j.jep.2023.116849
26. Zheng Z, Liu Y, Chen D, et al. Catalpol improved energy metabolism and inflammation through the SIRT5-mediated signaling pathway to ameliorate myocardial injury. *Sci Rep*. 2024;14(1):29240. doi:10.1038/s41598-024-80505-z
27. Li Z, Zhao J, Li H, Li Y, Lin C. Catalpol protects AC16 cells from hypoxia/reoxygenation injury by regulating the miR-22-3p/DPP4 axis. *J Biochem Mol Toxicol*. 2022;36(6):e23034. doi:10.1002/jbt.23034
28. Nemmar A, Beegam S, Zaaba NE, Alblooshi S, Alseiari S, Ali BH. The salutary effects of catalpol on diesel exhaust particles-induced thrombogenic changes and cardiac oxidative stress, inflammation and apoptosis. *Biomedicines*. 2022;10(1):99. doi:10.3390/biomedicines10010099
29. Lu R, Gu Y, Si D, Liu C. Quantitation of catalpol in rat plasma by liquid chromatography/electrospray ionization tandem mass spectrometry and its pharmacokinetic study. *J Chromatogr B Analyt Technol Biomed Life Sci*. 2009;877(29):3589–3594. doi:10.1016/j.jchromb.2009.08.047
30. L-n WU, Lu R, Gu Y, C-x LIU, D-y SI. Pharmacokinetics and bioavalibability of catalpol in rats. *Chin J Clin Pharmacol Ther*. 2012;17(2):126.
31. Xue B, Ma B, Zhang Q, et al. Pharmacokinetics and tissue distribution of Aucubin, Ajugol and Catalpol in rats using a validated simultaneous LC-ESI-MS/MS assay. *J Chromatogr B Analyt Technol Biomed Life Sci*. 2015;1002:245–253. doi:10.1016/j.jchromb.2015.08.026
32. Dąbrowska M, Souto EB, Nowak I. Lipid nanoparticles loaded with iridoid glycosides: development and optimization using experimental factorial design. *Molecules*. 2021;26(11):3161. doi:10.3390/molecules26113161
33. Narumi K, Miyakawa R, Ueda R, et al. Proinflammatory proteins S100A8/S100A9 activate NK cells via interaction with RAGE. *J Immunol*. 2015;194(11):5539–5548. doi:10.4049/jimmunol.1402301
34. Ostrand-Rosenberg S, Huecksteadt T, Sanders K. The Receptor for Advanced Glycation Endproducts (RAGE) and its ligands S100A8/A9 and High Mobility Group Box Protein 1 (HMGB1) Are key regulators of myeloid-derived suppressor cells. *Cancers*. 2023;15(4):1026. doi:10.3390/cancers15041026
35. Wautier MP, Chappey O, Corda S, Stern DM, Schmidt AM, Wautier JL. Activation of NADPH oxidase by AGE links oxidant stress to altered gene expression via RAGE. *Am J Physiol Endocrinol Metab*. 2001;280(5):E685–94. doi:10.1152/ajpendo.2001.280.5.E685
36. Wang S, Song R, Wang Z, Jing Z, Wang S, Ma J. S100A8/A9 in Inflammation. *Front Immunol*. 2018;9:1298. doi:10.3389/fimmu.2018.01298
37. Ma L, Sun P, Zhang JC, Zhang Q, Yao SL. Proinflammatory effects of S100A8/A9 via TLR4 and RAGE signaling pathways in BV-2 microglial cells. *Int J Mol Med*. 2017;40(1):31–38. doi:10.3892/ijmm.2017.2987
38. Araki K, Kinoshita R, Tomonobu N, et al. The heterodimer S100A8/A9 is a potent therapeutic target for idiopathic pulmonary fibrosis. *J Mol Med*. 2021;99(1):131–145. doi:10.1007/s00109-020-02001-x
39. He J, Wei L, Tan S, et al. Macrophage RAGE deficiency prevents myocardial fibrosis by repressing autophagy-mediated macrophage alternative activation. *FASEB j*. 2023;37(11):e23259. doi:10.1096/fj.202300173RR
40. Zhang L, He J, Wang J, et al. Knockout RAGE alleviates cardiac fibrosis through repressing endothelial-to-mesenchymal transition (EndMT) mediated by autophagy. *Cell Death Dis*. 2021;12(5):470. doi:10.1038/s41419-021-03750-4
41. Gao W, Zhou Z, Liang B, et al. Inhibiting receptor of advanced glycation end products attenuates pressure overload-induced cardiac dysfunction by preventing excessive autophagy. *Front Physiol*. 2018;9:1333. doi:10.3389/fphys.2018.01333
42. Paradela-Dobarro B, Fernández-Trasancos Á, Bou-Teen D, et al. Evolution and bad prognostic value of advanced glycation end products after acute heart failure: relation with body composition. *Cardiovasc Diabetol*. 2017;16(1):115. doi:10.1186/s12933-017-0598-3
43. Paradela-Dobarro B, Agra RM, Álvarez L, et al. The different roles for the advanced glycation end products axis in heart failure and acute coronary syndrome settings. *Nutr Metab Cardiovasc Dis*. 2019;29(10):1050–1060. doi:10.1016/j.numecd.2019.06.014
44. Li S, Hu D, Hu S, et al. Association of rs2070600 in advanced glycosylation end-product specific receptor with prognosis of heart failure. *ESC Heart Fail*. 2020;7(6):3561–3572. doi:10.1002/ehf2.12769
45. Guan L, Mao Z, Yang S, et al. Dioscin alleviates Alzheimer's disease through regulating RAGE/NOX4 mediated oxidative stress and inflammation. *Biomed Pharmacother*. 2022;152:113248. doi:10.1016/j.biopha.2022.113248
46. Mohammadzadeh A, Gol A, Kheirandish R. Effects of garlic (Allium sativum L) and Citrullus colocynthis (L.) Schrad individually and in combination on male reproductive damage due to diabetes: suppression of the AGEs/RAGE/Nox-4 signaling pathway. *BMC Complement Med Ther*. 2024;24(1):149. doi:10.1186/s12906-024-04402-8
47. Zhang Y, Murugesan P, Huang K, Cai H. NADPH oxidases and oxidase crosstalk in cardiovascular diseases: novel therapeutic targets. *Nat Rev Cardiol*. 2020;17(3):170–194. doi:10.1038/s41569-019-0260-8
48. Takaguri A, Shinohe S, Noro R, et al. SR9009 attenuates TGF-β1-induced renal fibrotic responses by inhibiting the NOX4/p38 signaling pathway in NRK-49F cells. *Eur J Pharmacol*. 2025;987:177162. doi:10.1016/j.ejphar.2024.177162

49. Lin H, He K, Zhang S, et al. Targeting G6PD to mitigate cartilage inflammation in TMJOA: the NOX4-ROS-MAPK axis as a therapeutic avenue. *Int Immunopharmacol*. 2024;139:112688. doi:10.1016/j.intimp.2024.112688
50. Wang L, He C. Nrf2-mediated anti-inflammatory polarization of macrophages as therapeutic targets for osteoarthritis. *Front Immunol*. 2022;13:967193. doi:10.3389/fimmu.2022.967193
51. Wang Z, Ren Y, Zhang D, et al. Elevated K(Ca)3.1 expression by angiotensin II via the ERK/NF-κB pathway contributes to atrial fibrosis. *J Mol Cell Cardiol*. 2025;202:133–143. doi:10.1016/j.yjmcc.2025.03.009
52. Yuan P, Liu J, Xiong S, et al. Effects and mechanism of Compound Qidan Formula on rats with HFpEF induced by hypertension and diabetes mellitus based on Ang II/TGF-β1/Smads signaling pathway. *J Ethnopharmacol*. 2023;313:116558. doi:10.1016/j.jep.2023.116558
53. Gonçalves PR, Nascimento LD, Gerlach RF, Rodrigues KE, Prado AF. Matrix metalloproteinase 2 as a pharmacological target in heart failure. *Pharmaceuticals*. 2022;15(8):920. doi:10.3390/ph15080920
54. She Y, Shao CY, Liu YF, Huang Y, Yang J, Wan HT. Catalpol reduced LPS induced BV2 immunoreactivity through NF-κB/NLRP3 pathways: an in vitro and in silico study. *Front Pharmacol*. 2024;15:1415445. doi:10.3389/fphar.2024.1415445
55. Feng ZJ, Wang LS, Ma X, et al. Catapol attenuates the aseptic inflammatory response to hepatic I/R injury in vivo and in vitro by inhibiting the HMGB1/TLR-4/NF-κB signaling pathway via the microRNA-410-3p. *Mol Immunol*. 2023;164:66–78. doi:10.1016/j.molimm.2023.11.004